H_2 production from formic acid over highly stable and efficient Cu-Fe-O spinel based photocatalysts under flow, visible-light and at room temperature conditions

Hanen Abdelli, Houeida Issa Hamoud, Juan Pablo Bolletta, Arnold Paecklar, Afrah Bardaoui, Krassimir L. Kostov, Ewelina Szaniawska, Antoine Maignan, Christine Martin, Mohamad El-Roz

H_2 Production from Formic Acid over Highly Stable and Efficient Cu-Fe-O spinel Based Photocatalysts under Flow, Visible-Light and at Room Temperature Conditions

Hanen Abdelli[a,b,c]†, Houeida Issa Hamoud[a]†, Juan Pablo Bolletta[d], Arnold Paecklar[d], Afrah Bardaoui[b], Krassimir L. Kostov[e], Ewelina Szaniawska[f], Antoine Maignan[d], Christine Martin[d], Mohamad El-Roz[a*]

[a]*Laboratoire Catalyse et Spectrochimie, Normandie Université, ENSICAEN, UNICAEN, CNRS, 14050 Caen, France.*
[b]*Laboratory of Nanomaterials and Systems for Renewable Energies (LaNSER), Research and Technology Centre of Energy (CRTEn), 2050 Hammam-Lif, Tunisia.*
[c]*Faculty of Sciences of Tunis (FST), University of Tunis El Manar, 2092, Tunis, Tunisia.*
[d]*Laboratoire CRISMAT, Normandie Université, ENSICAEN, UNICAEN, CNRS, 14050 Caen, France.*
[e]*Bulgarian Academy of Sciences, Institute of General and Inorganic Chemistry, 1113 Sofia, Bulgaria.*
[f]*Department of Physical and Macromolecular Chemistry, Faculty of Science, Charles University in Prague, Hlavova 8, 128 43 Prague 2, Czech Republic.*

∗Corresponding authors.

E-mail address: mohamad.elroz@ensicaen.fr, christine.martin@ensicaen.fr

Abstract

Catalytic dehydrogenation of liquid organic hydrogen carriers (LOHC), such as formic acid (FAc), is considered as a promising approach to safely store and easily transport hydrogen at ambient conditions. Generally, this process suffers from low activity, low reaction selectivity, low stability of the catalysts and/or the use of noble-metal based catalysts. In this study, a highly efficient $CuFe_2O_4$-based photocatalyst is reported for the photocatalytic dehydrogenation of FAc under visible light at room temperature and under continuous gas flow. The effects of various factors such as composition of the catalysts and thermal pretreatment are investigated along a series of samples. The synthesis, dispersion, oxidation states, photo-electrochemical properties and performances of these materials were investigated in details. A synergetic effect, with relatively high dehydrogenation selectivity (77% with 6.6 $mmol.g^{-1}.h^{-1}$ of H_2 production) is obtained on the copper-rich samples without any significant deactivation for two cycles of 20h/cycle. This study opens up a new route to design new Cu-based photocatalysts as cost-effective materials for visible-light driven photocatalytic dehydrogenation of FAc at room temperature.

Keywords: Photocatalysis, Hydrogen, LOHC, Formic acid, Dehydrogenation.

1. Introduction

Hydrogen represents a clean and promising energy vector which can efficiently replace the widely used fossil fuels. However, hydrogen generation from renewable sources under mild conditions and its storage in a safe and reversible manner remains challenging [1]. In this respect, formic acid (FAc), as a liquid organic hydrogen carrier (LOHC), is an excellent candidate for hydrogen storage due to its non-toxic character, its stability and its high hydrogen content (4.4 wt.%) [2]. Furthermore, FAc is readily available from sources such as biomass reforming, CO_2 hydrogenation and as a by-product/product of the chemical industry [3]. Its decomposition can proceed by two ways:

- Dehydrogenation : $HCOOH \rightarrow H_2 + CO_2$ (1)

and

- Dehydration : $HCOOH \rightarrow CO + H_2O$ (2)

Traditionally, expensive noble-metal based materials (i.e. Pd, Au, Ag, Pt) are used to achieve an acceptable conversion of FAc into H_2 [4,5,6,7,8,9]. Some of these systems operate at relatively high temperatures (100-350°C) which lead to a negative energy balance (the energy involved in the process is being higher than that elaborated from the produced hydrogen) [10]. Thereby, the selective photocatalytic dehydrogenation of FAc at room temperature (RT) using renewable source of energy (sun/visible light) has recently emerged as an outstanding alternative to the traditional thermal catalysts. Aside from noble metal-based photocatalysts, the utilization of low-cost systems such as heterojunctions (CdS/Fe_2O_3, MoS_2/CdS, Ni-Co/CdS, $Ni_2P/Zn_3In_2S_6$, $MoP/Zn_3In_2S_6$, etc.) [11,12], layered

[13] or core-shell structures (CdS/TNT, CdS@ZIF-8, CdS–ZnS, etc.) [14,15,16] has shown enhanced performances ascribed to the efficient electron–hole pair separation. Among these systems, there have been only few studies reporting the use of visible-light responsive copper-based photocatalysts for hydrogen production from FAc [17,18,19]. In addition, most of these studies investigate the photo-reforming of FAc in the liquid phase, where the photocatalyst's instability at low pH is the main drawback (oxidation of sulfur-based catalysts, metal leaching, etc.) [17,18,19]. Recently, Zhang et *al.* investigated binary CuO/TiO_2 heterojunction nanofibers for FAc photo-reforming in liquid phase under simulated sunlight irradiation at RT [18]. It was found that hydrogen production (2 $mmol.g^{-1}.h^{-1}$) begins after 2 h of irradiation, defined as the induction period, due to the photo-assisted reconstruction of binary heterojunctions (CuO/TiO_2) into a quaternary ($Cu/Cu_2O/CuO/TiO_2$) system. More recently, a very cheap and simple CuO/TiO_2 mixture has been used to produce hydrogen by solar light irradiation from a FAc solution at pH = 2.5 [19]. The system was able to produce 2.4 $mmol.g^{-1}.h^{-1}$ of H_2 in the first cycle (1 day) but reduced to 1.6 $mmol.g^{-1}.h^{-1}$ after five cycles (5 days) due to the Cu leaching.

Alternatively, we have investigated a metal organic framework (MOFs) based materials for photocatalytic dehydrogenation of FAc [20]. The post-metalation of the MOFs structure with Cu and the in-situ restructuring of this latter during the reaction accounted for its high activity and the high selectivity of the reaction. However, the investigation of new copper-based catalysts, for FAc dehydrogenation, that can be easily synthesized from earth-abundant elements, such as Cu and Fe, is still of great interest due to the complexity and the cost of both synthesis procedure and activation process of MOF-based structures.

Therefore, and to overcome the previous cited limitations, we aim in this work to investigate the dehydrogenation of FAc in vapor phase under continuous flow over low-cost and one-pot synthesized iron-copper oxide based photocatalysts. In this context, the $CuFe_2O_4$ spinel is a material which attracts much attention in photocatalysis due to its

effectiveness under visible light irradiation, redox properties, non-toxicity, low cost, room-temperature magnetic behavior and high charge transfer [21,22,23]. To date, $CuFe_2O_4$ was mainly used for the photocatalytic degradation of organic effluent in the presence of H_2O_2, (Fenton-like reaction) [21-27] and water splitting [28]. Herein, we investigate for the first time the photocatalytic activity and stability of $CuFe_2O_4$-based systems for a vapor-phase dehydrogenation of FAc under visible-light irradiation at room temperature. The stability of the photocatalysts, the effect of Cu:Fe ratio and the impact of the thermal treatment used to prepare the materials were tested during this reaction. The nominal Cu:Fe ratios (1:11, 1:3, 1:2, and 2:1) are used in the following as a labeling of the samples for more clarity. The preparation of the samples, the physicochemical and photo-electrochemical properties of the catalysts were deeply inspected using *in-situ* X-ray powder diffraction (XRPD), scanning electron microscopy coupled with energy dispersive X-ray (SEM-EDX), UV-Vis diffuse reflectance (DR-UV-Vis), X-ray photoelectron spectroscopy (XPS) and potentiometry. Then, the photocatalytic activity is explored using Fourier transform infrared (FTIR) *operando spectroscopy*. Finally, a tentative mechanism of the reaction is proposed.

2. Experimental part

2.1. Materials

Iron nitrate ($Fe(NO_3)_3 \cdot 9H_2O$; ≥98%), copper nitrate ($Cu(NO_3)_2 \cdot 3H_2O$; ≥99.99%), sodium hydroxide pellets (≥99.9%), maize starch ($(C_6H_{10}O_5)_n$), ascorbic acid (≥99%), formic acid (≥99%) and acetic acid (≥99.8%) were all purchased from Sigma Aldrich. Distilled water and absolute ethanol were used as solvents. Commercial SiO_2 (Ultrasil 5500 GR) and Fe_2O_3 (99.5%) were used as received from Evonik-Degussa and Alfa Aesar, respectively.

2.2. Catalyst synthesis

It should be noted that all the syntheses reported in this study were reproduced at least twice to attest of their reproducibility.

Synthesis of $CuFe_2O_4$-based catalysts with Cu:Fe ratios 1:11, 1:3, 1:2, and 2:1:

These samples were synthesized by the starch-assisted sol-gel auto-combustion method [29]. The desired amounts of iron nitrate and copper nitrate were dissolved in distilled water to obtain a homogeneous solution. Then, an aqueous solution of starch $(C_6H_{10}O_5)_n$ was mixed with the metal-nitrate solution. The obtained mixture was heated at 100°C under continuous stirring until the formation of a viscous brown gel. Then, the gel was heated at 180°C for 4 h to initiate a self-sustaining combustion reaction and produce the precursor. The precursors were further ground to powder, and finally heated in air at various temperatures as described in the following (*section 3*).

Synthesis of CuO, Cu_2O, Cu_2O/Cu^0 (used as reference material):

CuO was synthetized using a chemical precipitation method described elsewhere [30]. $Cu(NO_3)_2$ solution (300 mL 0.02 M) was prepared and heated at 100°C under vigorous stirring. Then, 0.5 g of solid NaOH was rapidly added resulting in the production of a considerable amount of black precipitates. Next, the precipitates were heated at 100°C for 20 min under ambient atmosphere. The resulting products were then centrifuged, washed with water and ethanol several times, and then dried in air at room temperature.

Cu_2O was synthetized using a hydrothermal method described elsewhere [31]. $Cu(NO_3)_2 \cdot 3H_2O$ (181.2 mg) was dissolved in 30 mL of anhydrous absolute ethanol in a Teflon flask under vigorous stirring. After dropwise addition of acetic acid (1.5 mL), the solution was ultrasonicated for 5 min and transferred to a Teflon-lined stainless-steel autoclave (capacity 40 mL) to reach 80% filling. The reaction was performed at 180°C for 2 h. The brick red powder was then collected and washed several times with distilled water and ethanol, and dried in air at 60°C for 12 h.

In a typical procedure for the synthesis of Cu_2O/Cu [32], 0.4 g of NaOH was added to 100 mL of 0.1 M $Cu(NO_3)_2 \cdot 3H_2O$ under magnetic stirring. After complete dissolution of NaOH, 2 g of ascorbic acid were added and stirred for 30 min at room temperature. During the

process, the color of the solutions changed from blue to brown colors. The precipitate was washed several times with water and ethanol and finally dried overnight at 60°C.

2.3. Characterization

XRPD analysis of Cu:Fe oxides as well as the reference materials (CuO, Cu_2O, Cu_2O/Cu^0 and Fe_2O_3, Fig. S 1) were carried out in PANalytical X'Pert Pro diffractometers with either Co Kα1/ Kα2 (λ = 1.7892 Å/1.7932 Å with ratio 0.5) or Cu Kα1 irradiation (λ = 1.5406 Å) at room temperature. Additional XRPD patterns were collected during *in situ* high-temperature synthesis in a Rigaku SmartLab diffractometer, equipped with a rotating anode source (45 kV, 200 mA, λ = Cu Kα1/Kα2 with ratio 0.4970) and a HyPix-3000 detector in 1D mode. Measurements were performed in Bragg-Brentano geometry at constant temperatures and also while heating from 500 to 900°C at a 1°C.min^{-1} rate in an Anton Paar XRK900 chamber, with an Inconel sample holder. For these *in-situ* experiments, the precursors were previously heated *ex-situ* at 500°C overnight under air to avoid uncontrolled combustions in the reaction chamber of the diffractometer.

Nitrogen adsorption/desorption measurements were performed with an ASAP 2020 MP instrument. The specific surface area was calculated with the Brunauer-Emmett-Teller (BET) equation, while the pore volumes were determined by the Barrett-Joyner-Halenda (BJH) method (Table S1). Prior to the measurements, samples were degassed *in vacuum* at 300 ºC for 3 h.

The content and distribution of Cu and Fe were determined by SEM-EDX on a JEOL JSM-5500LV microscope or a MIRA TESCAN microscope (Table S1). The images were collected with an acceleration voltage of 30 kV. Advanced transmission electron microscopy (TEM) was carried out on an aberration probe, and image corrected JEM ARM200F cold FEG microscope operated at 200 kV equipped with a CENTURIO EDX detector and GIF Quantum spectrometer. The metal contents were also verified by a Varian

ICP-OES 720-ES inductively coupled plasma spectrometry (ICP). The Cu:Fe ratios measured by ICP (Table S1) confirm the nominal ones.

XPS measurements were carried out on an AXIS Supra electron spectrometer (Kratos Analytical Ltd.) with base vacuum in the analysis chamber in the order of 10^{-8} Pa. The samples were irradiated with monochromatized Al Kα radiation with photon energy of 1486.6 eV. The photoemitted electrons were separated according to their kinetic energy by a 180 o-hemispherical analyzer with a total instrumental resolution of 0.6 eV (as measured by the FWHM of Ag $3d_{5/2}$ line) at pass energy of 20 eV. Energy calibration was performed by normalizing the C 1s line of adventitious adsorbed hydrocarbons on silver folio to 284.6 eV. The analysis area was 700x300 μm^2. DR-UV-Vis measurements relevant to Cu speciation were carried using a Cary 4000 UV-Vis spectrophotometer and a HARRICK Praying Mantis diffuse reflectance accessory. All spectra were recorded between 200-800 nm using an average time of 0.2 s and a scan rate of 300 $nm.min^{-1}$.

Both electrochemical and photoelectrochemical experiments were performed by using a potentiostat Autolab PGSTAT302N in two-compartment cell and in three-electrode configuration. The cathodic compartment was physically separated from the anodic one by a proton exchange membrane (Nafion 117; thickness 0.007 in). The fluorine-doped tin oxide covered glass (FTO) was utilized as a conductive substrate for working electrode (geometric area 0.71 cm^2), Pt wire was applied as counter electrode and mercury sulfate electrode (Hg/Hg_2SO_4/sat. K_2SO_4) as reference electrode. Potentials were converted to the reversible hydrogen electrode (RHE) reference scale. The aqueous electrolyte solutions used were 0.1 $mol.dm^{-3}$ Na_2SO_4 at pH = 6.4 after saturation in argon. For photoelectrochemical experiments, the solar simulator (Quantum Design Model LSE341) used as a light source is equipped with 300 W Xe lamp (light intensity = 100 $mW.cm^{-2}$) and AM 1.5 Global filter. The photocurrent vs. time curves were measured with a potential sweep of 10 mVs^{-1} at the imposed potential of 0.0V vs. RHE under chopped light. The electrochemical experiments

were performed by scanning the potential from 1.02 V to 0.0 V vs. RHE (at 10 $mV.s^{-1}$). Catalyst solutions were prepared by suspending 10 mg of photocatalyst in a mixture of 20 µL Nafion solution (0.5 wt%) and 200 µL of ethanol followed by sonification for 30 min. Thereafter, 20 µL of the sample solution was pipetted onto the FTO surface (geometric area 0.71 cm^2) followed by drying at 80°C for 10 min.

2.4. Photocatalytic test

For the *operando* experiments, a 'sandwich-like' IR cell-reactor (scheme S1) was used to study the performances of the different Cu-Fe based materials during the photodecomposition of formic acid under visible light irradiation at room temperature (25 °C), as detailed in Ref. [33,34]. Due to magnetic aggregation in some of the samples, it was difficult to prepare a self-supported pellet. Thus, the powders were mixed (50/50 wt.%) with an inert/non-active SiO_2 support (Ultrasil 5500 GR, Evonik-Degussa) for preparing thin pellets of ≈ 20 mg. The catalyst was activated in argon gas at RT under visible irradiation using a Xe lamp (LC8 Hamamatsu, 71 $mW.cm^{-2}$ of irradiance) with a pass-high filter >390 nm. Then, the reaction was studied in the presence of 2600 ppm of FAc (0.26 vol.%) with a total flow rate of 25 $cm^3.min^{-1}$ in argon. The relative concentrations of the effluent gases were stabilized before being sent to the cell, then an adsorption step of FAc on the catalyst surface was performed under dark conditions. Finally, the composition of the output gas from the IR reactor cell was analyzed simultaneously by mass spectrometry (MS) (Quadrupole Pfeiffer Omnistar GSD 301) and IR spectroscopy (ThermoNicolet NEXUS 670 FTIR) equipped with a mercury cadmium telluride (MCT) detector with a spectral resolution of 4 cm^{-1} and accumulating 64 scans. The evolution of FAc concentration in the gas phase was monitored using the surface area of IR band at 1109–1101 cm^{-1} and the FAc MS signal (m/z = 45 and 46). The selectivity of CO_2 and CO were determined using the IR band areas at 2395-2182 cm^{-1} and 2140-2020 cm^{-1}, respectively. The amounts of hydrogen were determined using the MS signal at m/z = 2 after correction from water contributions

and the results were confirmed by online gas chromatography (GC) analysis of the gas phase products at the steady-state using a Compact GC$^{4.0}$ equipped with 3 analysis channels. The first thermal conductivity detector (GC-TCD, Interscience) is equipped with a Molseive5 A (25 m × 0.32 mm) and Rt-QBond (3 m × 0.32 mm) columns for respectively analyzing of O_2, N_2, CH_4, CO and CO_2 using helium as a carrier gas. The second TCD channel is equipped with Rt-QBond (3 m × 0.32 mm) and argon as a carrier gas for H_2 analysis. The third channel with flame ionization detector (FID) and He as carrier gas equipped with Rt-QBond (25 m × 0.32 mm) column for hydrocarbons (HC) detection (C_1-C_6). The peak areas of CO_2, CO and H_2 were converted into concentrations by using their calibration curves (Fig. S 2) (operating conditions: split flow rate = 5 mL.min^{-1} for both TCD and 10 mL.min^{-1} for FID; inlet temperature 80°C; column temperature 60°C for O_2, N_2, CH_4, CO and CO_2, 50°C for H_2 and 45°C for HC).

The FAc conversion (expressed in % or mmol per g of photocatalyst per hour per irradiated surface) and the selectivity (%) were calculated from Equations 3-6, at the steady-state using the calibration curve for different products of the reaction (Fig. S 2). The apparent quantum yield was calculated using the actinometer method as detailed in the SI (Fig. S 3). It should be noted that the irradiated surface of the pellet is about 1.6 cm^2. The FAc conversion and conversion rates are calculated as follows:

$$\text{FAc conversion (\%)} = \frac{[\text{FAc}]_0\ (\text{ppm}) - [\text{FAc}]_t\ (\text{ppm})}{[\text{FA}]_0\ (\text{ppm})}\ \text{x}\ 100 \quad (3)$$

$$\text{Conversion rate}\ (\text{mmol.g}^{-1}.\ \text{h}^{-1}) = \frac{\text{Total flow}(\text{L.h}^{-1})\ \text{x}\ [\text{FAc}]0\ (\text{ppm})\ \text{x}\ 10^{-6}\ \text{x}\ \frac{\text{conversion \%}}{100}\ \text{x}\ 1000}{\text{M}_{\text{FAc}}(\text{g.mol}^{-1})\ \text{x}\ \frac{1}{\text{d}_{\text{FAc}}}(\text{L.g}^{-1})\ \text{x}\ \text{m}_{\text{catalyst}}(\text{g})} \quad (4)$$

$$\text{Conversion in mmol.g}^{-1}.\ \text{h}^{-1}.\text{cm}^{-2} = \frac{\text{Conversion rate (mmol.g}^{-1}.\ \text{h}^{-1})}{\text{S}_{\text{irradiated}}(\text{cm}^2)} \quad (5)$$

$$\text{Selectivity (\%)} = \frac{\text{Concentration of target product (ppm)}}{\text{Concentration of FAc converted (ppm)}}\text{x}100\ \text{, with target product} = H_2/CO_2 \text{ or CO} \quad (6)$$

3. Results and discussion

3.1. Catalysts Characterizations

To guide the preparation of samples starting from precursors prepared by sol-gel, *in-situ* XRPD experiments were conducted on samples with Cu:Fe ratio 1:2 and 1:3. The full results are shown in Fig. 1A and 1E up to 800°C, respectively. No further changes were observed above this temperature beyond the expected thermal expansion of the materials. These temperature-dependent plots show that the initial mixes (at 600°C) already contain phases similar to the desired $CuFe_2O_4$ spinel together with the binary oxides Fe_2O_3 and CuO. The $CuFe_2O_4$ spinel undergoes a reversible structural phase transition from tetragonal (space group $I4_1/amd$) to cubic (space group $Fd\text{-}3m$) at approximately 390°C [35], meaning that in Fig. 1 all spinel peaks are indexed in the high-temperature cubic phase. In the sample with Cu:Fe ratio 1:2 (Fig. 1A), the peaks of the binary oxides markedly decrease with heating until disappearing above 720°C (Fig. 1B and 1D), concurrently with an increase in the intensities and decrease in the width of the Bragg peaks corresponding to $CuFe_2O_4$ (Fig. 1C), usually associated with an increase of the amount of phase and of its crystallinity, respectively. In this sample prepared from a precursor with Cu:Fe ratio 1:2, only traces of CuO can be detected after the high-temperature treatment, resulting in a product consisting of an overwhelming majority of $CuFe_2O_4$. On the other hand, for the material obtained from the Cu:Fe 1:3 precursor (Fig. 1E), peaks of Fe_2O_3 only decrease up to 800°C (Fig. 1F and 1H), without completely disappearing. This shows a similar formation of the $CuFe_2O_4$ spinel, with the excess of Fe from the precursor (compared to the $CuFe_2O_4$ formula) remaining as additional Fe_2O_3 until very high temperatures (900°C) (Fig. 1F). In this sample and contrary to the observations of the Cu:Fe 1:2 sample, no excess of CuO is detected after the high-temperature treatment (Fig. 1H). These results demonstrate that changing the Cu:Fe

ratio from 1:2 to 1:3 drastically modifies the final constituents of the samples after thermal treatments. Heating mixtures of copper and iron oxides outside the 1:2 Cu:Fe ratio always results in $CuFe_2O_4$ plus an excess of the more abundant binary oxide. This is in accordance with early observations by Milligan and Holmes [36] who showed that non-stoichiometry does not occur in this spinel.

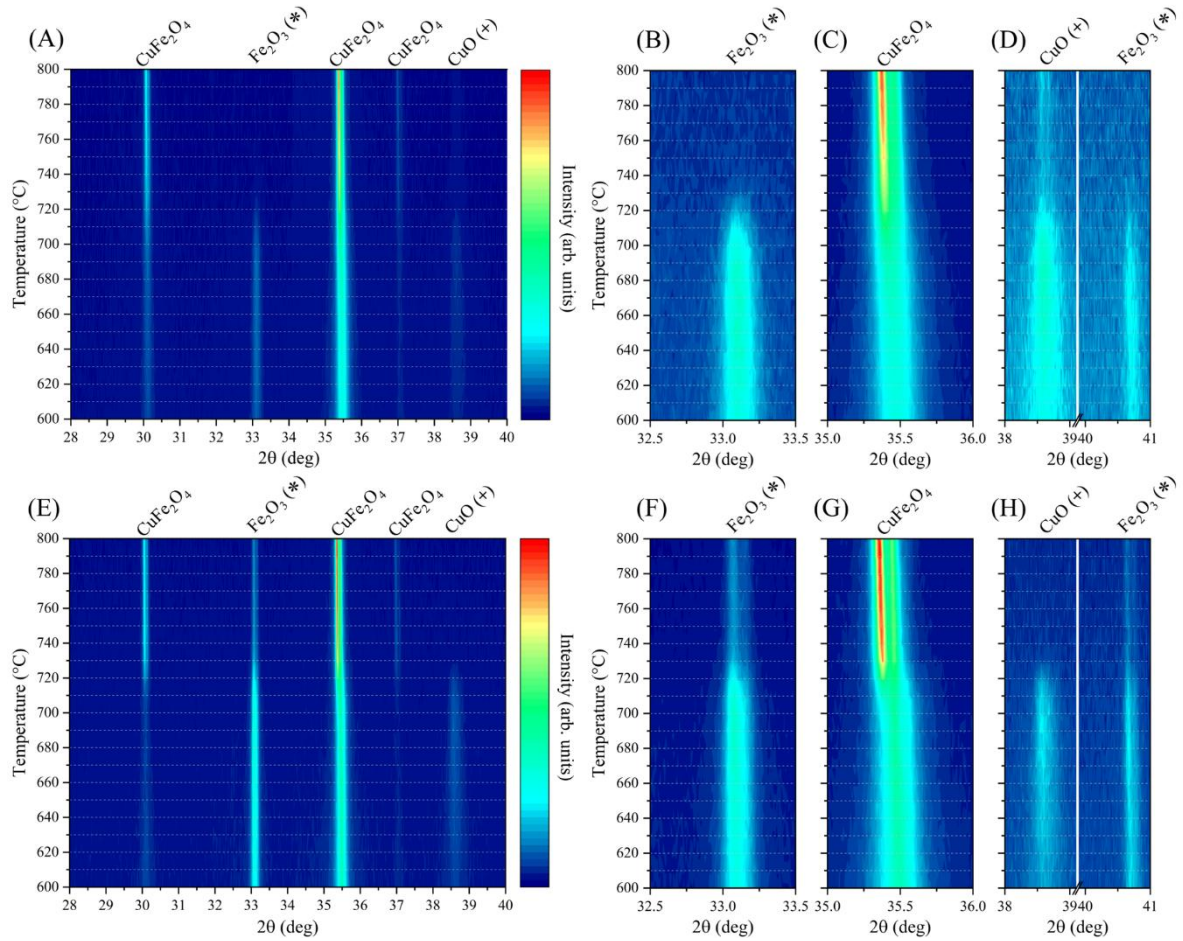

Figure 1. (A) Temperature-dependent XRPD for *in-situ* synthesis of $CuFe_2O_4$ from a Cu:Fe 1:2 precursor. (B-C-D) Details of peaks highlighting the evolution of Fe_2O_3, $CuFe_2O_4$ and CuO, respectively. (E) Temperature-dependent XRPD for *in-situ* synthesis from a Cu:Fe 1:3 precursor. (F-G-H) Details of peaks highlighting the evolution of Fe_2O_3, $CuFe_2O_4$ and CuO, respectively. Marked peaks correspond to Fe_2O_3 (*) ($R\bar{3}c$ space group) or CuO (+) ($C2/c$ space group). Arbitrary scales are independent between panels.

Considering the *in-situ* experiments, samples with different Cu:Fe ratios and thermal treatment temperatures were prepared *ex-situ* to obtain catalysts with or without excess of the binary oxides. The sample with Cu:Fe 1:11 (Fig. 2A) was prepared with a clear excess

of Fe in the mixture with respect to the ideal copper iron spinel composition, and thus results in a sample mainly composed of Fe_2O_3, together with a small amount of $CuFe_2O_4$. In a similar manner, results for the Cu:Fe 1:3 mixture always show a strong presence of Fe_2O_3 (Fig. 2B and 2C) regardless of thermal treatment. However, in contrast with the previous case, the spinel is the main phase in the high-temperature sample. In addition, CuO cannot be detected, suggesting that all Cu resides within the $CuFe_2O_4$ spinel. Results for Cu:Fe 1:2 are shown in Fig. 2D (600°C) and 2E (800°C). In the low-temperature sample, $CuFe_2O_4$ peaks are identifiable, with additional Fe_2O_3 and CuO. When the temperature is increased to 800°C, the $CuFe_2O_4$ spinel clearly becomes the main phase together with a trace amount of remaining CuO. Results for both *ex-situ* synthesis of Cu:Fe 1:2 and Cu:Fe 1:3 are in line with those obtained during *in-situ* experiments. As shown in Fig. 1E-F, the samples obtained from the Cu:Fe 1:3 precursor are always mixed with an excess of Fe_2O_3. This marks a strong difference between these two samples treated at high temperatures, as Cu:Fe 1:2 precursor produces samples with a negligible, trace amount of binary CuO, while the Cu:Fe 1:3 precursor generates a mixed sample with a marked presence of binary Fe_2O_3. An additional sample was prepared with Cu:Fe ratio 2:1, which is found to contain a large amount of CuO together with $CuFe_2O_4$ as a secondary phase, producing a sample in which most of the Cu now lies in the form of binary copper oxide.

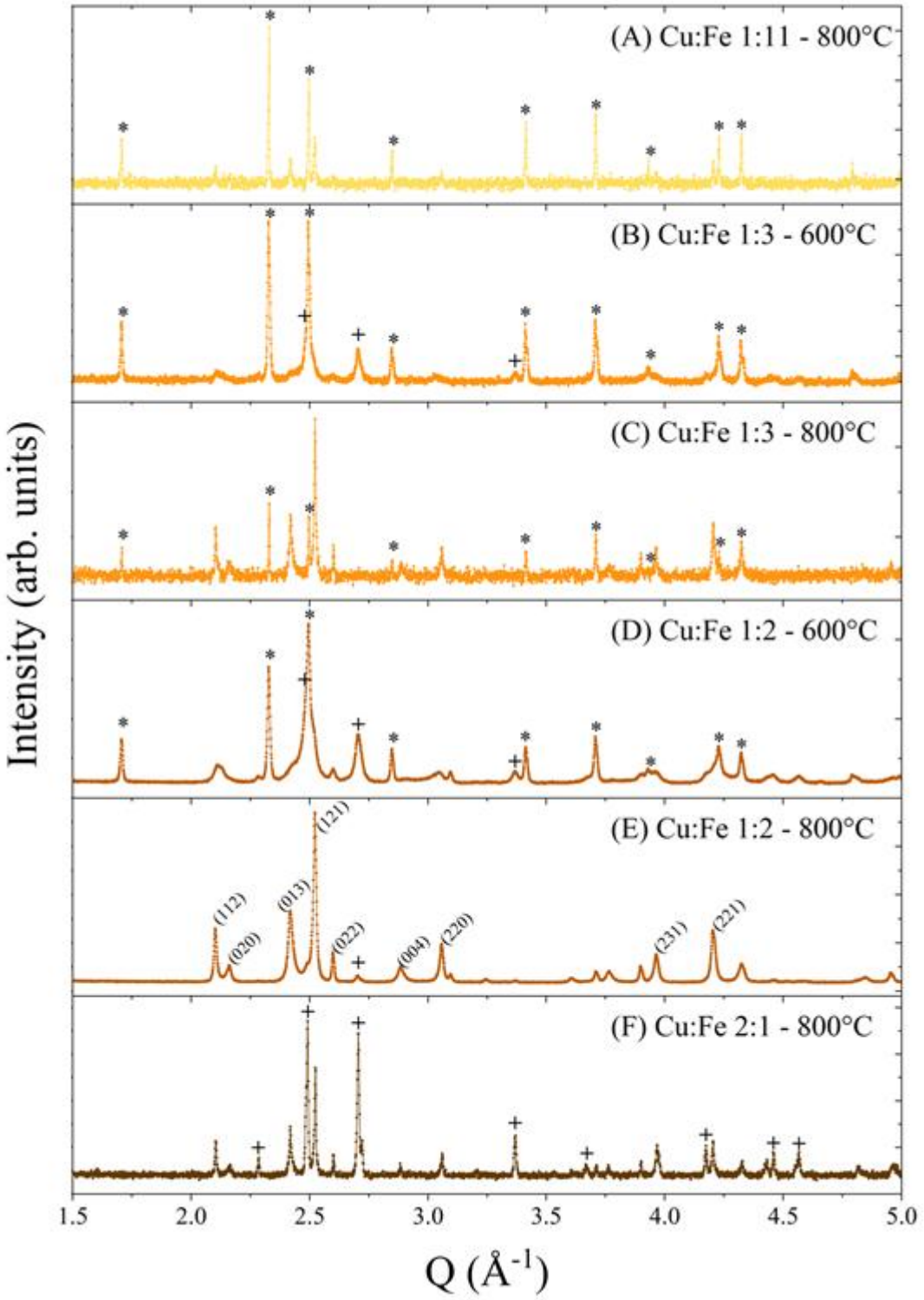

Figure 2. RT XRPD patterns for catalysts obtained from precursors with different Cu:Fe ratios and synthesis temperatures. Unmarked peaks correspond to $CuFe_2O_4$ (tetragonal, space group $I4_1/amd$), marked peaks correspond to Fe_2O_3 (*) ($R\bar{3}c$ space group) or CuO (+) ($C2/c$ space group). The indexation of the main Bragg peaks of the spinel is given in panel (E) as it corresponds to a near single-phase sample. As patterns were collected in different diffractometers with different X-ray sources, they are presented as a function of Q to facilitate the comparison.

The UV-Vis diffuse reflectance analysis of samples with various nominal Cu:Fe ratios and thus different constituents demonstrates that their optical behavior depends-on the involved phases (Fig. 3A and S 4). Starting from the Cu:Fe 1:11 sample, the increase of Cu content results in an increase of the band intensity at 567 nm, attributed to $CuFe_2O_4$ [37], with a redshift for the Cu:Fe 1:3 sample in respect to 1:11. An additional broad absorption band appears at around 690 nm for the 1:2 sample and becomes more intense for the 2:1 sample. It can be attributed to Cu^{2+} electron d–d transitions in distorted CuO_6 octahedra of CuO [38], as detected by XRPD. The presence of copper oxide in the Cu-rich samples is also confirmed by SEM (Fig. 3B). Contrary to the samples with Cu:Fe ratio lower than 1:2, the Cu:Fe 1:2 sample reveals the existence of copper oxide islands whose quantity increases in the 2:1 sample. The presence of excess of Cu in the Cu:Fe 1:2 was also confirmed by HR-TEM analysis (Fig. S5).

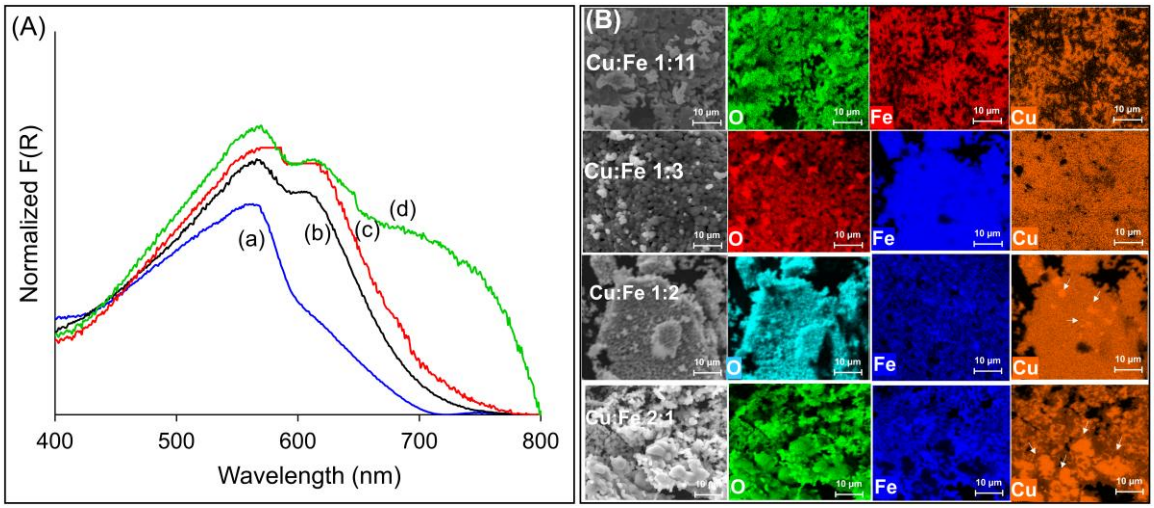

Figure 3. (A) DR-UV-Vis spectra of (a) 1:11, (b) 1:3, (c) 1:2 and (d) 2:1 Cu:Fe samples. (B) SEM and elemental mapping analysis of Cu:Fe 1:11, 1:3, 1:2 and 2:1 samples.

3.2. Photocatalytic activity

First, the photocatalytic reforming of FAc was investigated upon Cu:Fe 1:2 sample treated at 600°C and 800°C. The catalytic tests were conducted under visible light irradiation at room temperature with an initial FAc concentration of 2600 ppm (~0.26%) in Ar atmosphere and with total flow of 25 $cm^3.min^{-1}$. Each experiment was repeated at least two

times with an estimated relative error of less than 7%. The FAc conversions as well as the produced amounts of H_2, CO_2 and CO, and their corresponding selectivity are summarized in Table 1.

$CuFe_2O_4$ treated at 600°C shows very low activity while it is around 9 times higher for the same catalyst treated at 800°C and tested under similar conditions (Table 1). The dehydrogenation (Eq. 1) selectivity is about 77 % (Table 1, Fig. S 6-7) vs. 23% of dehydration (Eq. 2). The molar conversion rates of FAc are almost equal to the sum of CO_2 (or H_2) and CO, demonstrating the absence of other carbon beside products. This result reveals that the effect of the treatment temperature is very significant. As discussed previously, the composition of the two catalysts changes with the preparation temperature, as the 600°C sample still contains relatively high quantities of Fe_2O_3 and CuO, while only trace amounts of the latter remain in the 800°C sample; this explains their different photocatalytic behavior. Based on this, 800±25°C is chosen as the optimum calcination temperature of Cu-Fe spinel samples with different Cu:Fe ratio.

Table 1. Results of the activity and reaction selectivity of the FAc reforming at the steady state over the catalysts with different Cu:Fe ratios and treatment temperatures.[a]

Cu:Fe ratio (treatment temperature in °C)	Conv.%[b]	Conversion rate ($mmol.g^{-1}.h^{-1}.cm^{-2}$)[c]	H_2 ($mmol.g^{-1}.h^{-1}.cm^{-2}$)	CO_2 ($mmol.g^{-1}.h^{-1}.cm^{-2}$)	CO ($mmol.g^{-1}.h^{-1}.cm^{-2}$)	dehydrogenation selectivity (%)	apparent quantum yield %
1:11 (800)	1.5	0.17	n.d[d]	n.d	n.d	n.d	n.d
1:3 (800)	1.9	0.20	n.d	n.d	n.d	n.d	n.d
1:2 (600)	5.6	0.60	0.47	0.60	n.d	n.d	n.d
1:2 (800)	47.4	5.22	4.14	4.23	1.41	77	9.0
2:1 (800)	51.5	5.56	4.10	4.30	1.54	76	9.9

[a]Reaction conditions: [FAc]=2600 ppm (0.26%) in Ar; total flow 25 $cm^3.min^{-1}$; T=25 °C; Xe-lamp 150 W with visible light pass filter (λ>390 nm); irradiance=71 $mW.cm^{-2}$; mcat=10 mg+10mg of inert silica (self-supported pellet with irradiated surface of 1.6 cm^2); reaction time =17 h.
[b] relative conversion error is ± 7%
[c] unit expressed in mmol per g of catalyst (m_{cat}=10 mg) per hour per cm^2 of irradiated surface (1.6 cm^2). Values should be multiplied by 1.6 cm^{-2} for a rate in $mmol.g^{-1}.h^{-1}$.
[d]n.d. non determined (under the detection limit of the apparatus).

For better understanding the $CuFe_2O_4$ catalyst behaviors, additional photocatalytic tests have been performed over samples with Cu:Fe ratios 1:11, 1:3 and 2:1 after their calcination at 800 °C using similar reaction conditions to those for Cu:Fe (1:2). The results, assembled in Figure 4A and Table 1, demonstrate that samples with Cu:Fe 1:11, and 1:3 do not exhibit any significant activity towards H_2 production from formic acid (< 2%), revealing that samples with additional Fe_2O_3 have their photocatalytic activities noticeably hindered. This is confirmed by characterizing additional samples synthetized from a Cu:Fe ratio ranging between 1:11 and 1:3 (e.g. Cu:Fe = 1:5) that did not show any activity (the results are not shown here for the sake of brevity). From these preliminary results, it can be inferred that the presence of extra- spinel-structure Cu species beyond $CuFe_2O_4$ spinel is crucial for the photocatalytic activity of the samples (Cu:Fe (1:2) and (2:1)). However, it seems that the presence of extra-structure iron species (e.g. Fe_2O_3) didn't make the $CuFe_2O_4$ spinel photocatalytically active for the conversion of FAc (Cu:Fe (1:11), (1:5) and (1:3)). On the other hand, the similar results obtained over Cu:Fe (2:1) in respect to Cu:Fe (1:2) indicate that the excess of CuO (Cu:Fe 2:1) is not enhancing the photocatalytic activity. In what follows, we will focus on two main samples for highlighting the origin of the photocatalytic activity: the non-active Cu:Fe (1:3) and the highly active Cu:Fe (1:2).

The time-dependent FAc conversion over Cu:Fe 1:2 has been then investigated for two successive cycles with 20 h of visible light irradiation per cycle separated by 1 h of dark (Fig. 4B). The first cycle manifests an induction period before reaching a steady state after 1 h with similar profiles of FAc conversion and CO_2/H_2 production.

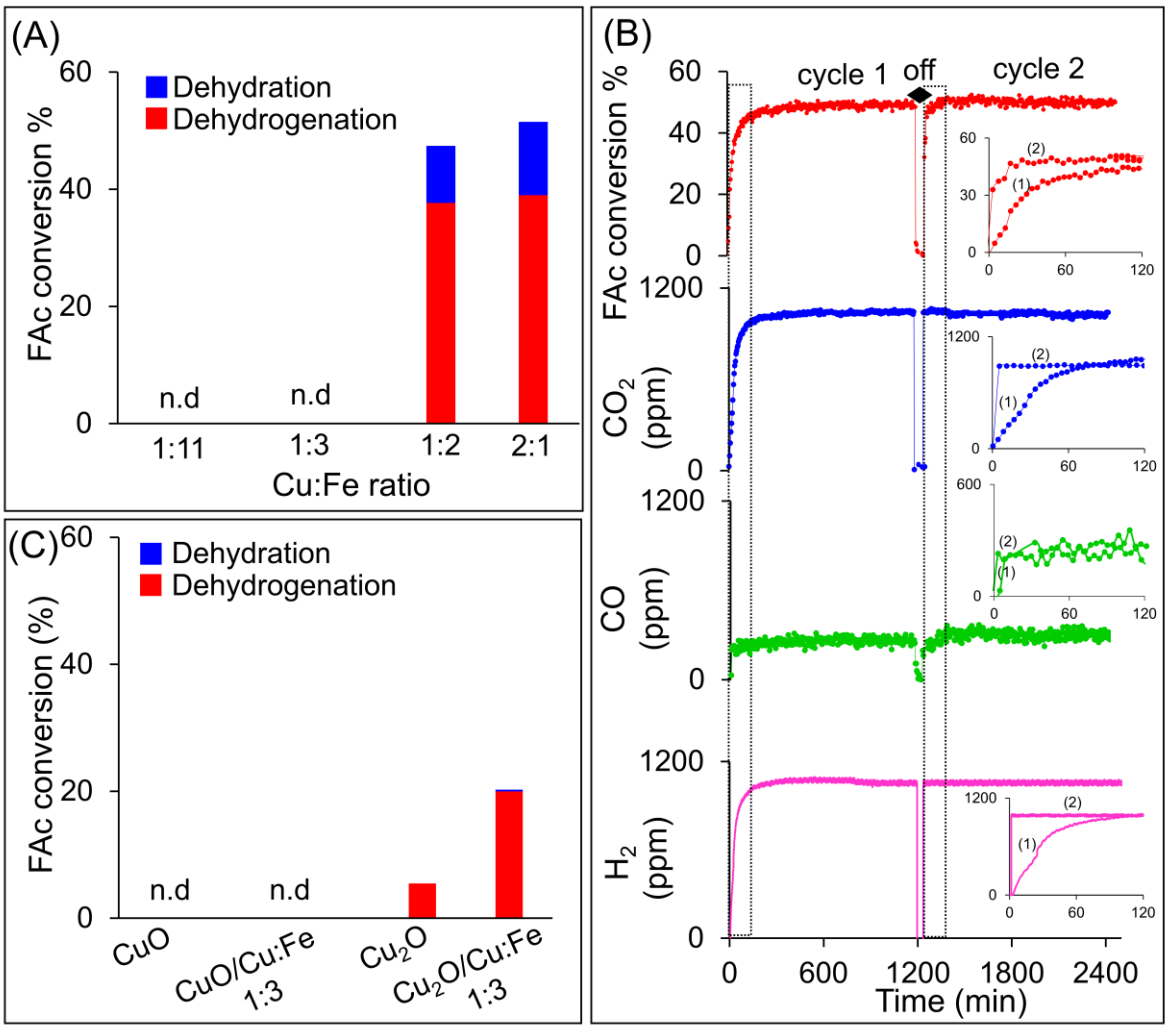

Figure 4. (A) FAc conversion (%) and the corresponding selectivity (%) at t = 17 h of reaction over samples with different Cu:Fe ratios treated at 800°C. (n.d = non detected) (B) Evolution of the FAc conversion (%) and the corresponding gas phase products (CO_2, CO and H_2) during the FAc photo-reforming over Cu:Fe 1:2 under visible irradiation at RT. Insert: zooming on the early period of the reaction during first (1) and second (2) cycle (doted zones). (C) FAc conversion (%) and the corresponding selectivity (%) at t = 17 h of reaction over CuO, Cu_2O and their 1:1 mixture with Cu:Fe 1:3.

A comparable behavior with an equivalent induction period is observed for the Cu:Fe 2:1 sample (Fig. S 8). The presence of an induction time indicates an *in-situ* structuring of the catalyst. Taking into account our recent work, Cu^{2+} reduction to $Cu^{+/0}$ clusters is very probable [20]. This induction period totally disappears in the 2nd cycle and the FAc conversion spontaneously reaches the steady state after irradiation (see Inserts Fig. 4B). Importantly, the results reveal the absence of any significant deactivation of the catalyst tested constantly for two days. To the best of our knowledge, this activity (around 6.6 $mmol.g^{-1}.h^{-1}$ of H_2 production) is the highest for a dehydrogenation of FAc under visible

light irradiation at room temperature when comparing to other Cu-based materials reported in literature (Table S 4). Nevertheless, it is important to mention that the comparison between different works is approximate and could not be absolute due to differences in various factors (liquid phase and batch vs. vapor phase and under flow condition (our work), reactor geometry, intensity, wavelength and surface of irradiation, reaction conditions, and the absence of information on the photocatalyst stability in some studies).

To gain further insight on the active sites of Cu:Fe 1:2 catalyst treated at 800°C, other Cu-containing oxides were considered and tested towards H_2 production from FAc under similar experimental conditions. Particularly, CuO and Cu_2O were tested separately and also in 1:1 mixtures with the Cu:Fe 1:3 catalyst. The Cu:Fe 1:3 sample was chosen due to the absence of extra-framework copper oxide. The results are presented in Fig 4C and summarized in Table S2. Even though CuO is characterized by narrow band gap and high absorption in visible range of solar spectrum [18,39], this oxide alone or in a mixture with Cu:Fe 1:3 does not show any H_2 generation. This is probably because of its unsuitable conduction band (CB) position (~ +0.35 V vs. NHE at pH = 3) situated below the reduction potential of H^+/H_2 (-0.18 V vs. NHE at pH = 3) (scheme S 2) [18]. Meanwhile, Cu_2O displays a low photocatalytic activity with 5.6 % of FAc conversion and almost 100% of dehydrogenation selectivity at the steady state (Fig. 4C). The low efficiency of Cu_2O is attributed to the fast recombination of electron-holes charge carriers (scheme S 2) [40]. However, the evolution of the conversion versus the irradiation time reveals a significant induction period without any photocatalytic activity for more than 3.5 h (vs. <1 h for Cu:Fe 1:2), followed with a progressive increase in the activity until reaching the steady state at ~5 h (Fig. 5A). Interestingly, a fourfold enhanced photocatalytic activity with respect to Cu_2O (5.6 % of FAc conversion) is obtained by mixing Cu_2O with Cu:Fe 1:3 (about 20 % of FAc conversion at steady state) with a shorter induction period (~0.5 h) and a similar behavior in the second cycle (Fig. 5A). Moreover, a minor amount of CO was detected for this mixture

(Fig. S 9), suggesting that CO production mainly occurred on copper iron spinel rather than on Cu_2O, being characterized by a high selectivity towards dehydrogenation. We should underline that these results could not be compared directly with the spinel-based samples as we used a high amount of Cu_2O (25 wt.%) in the mixture in order to provide a good dispersion and accessible Cu_2O/ferrite interface. Based on these results, we can assume that the spinel plays an important role and significantly enhances the photocatalytic activity of the system. Furthermore, spinel can stabilize the active copper sites, i.e. the activity of Cu:Fe 1:2 was not significantly changed after several months of aging time, contrary to Cu_2O. On the other hand, this result supports a possible restructuring of the Cu species under the reaction, e.g. formation of $Cu^{+/0}$. This hypothesis is supported by the inactivity of the spinel with a 1:3 Cu:Fe ratio, the inactivity of CuO and the induction time observed on Cu_2O and its decrease when the inactive 1:3 Cu:Fe spinel is used as support. This agrees with our recent study on the *in-situ* restructuring of Cu^{2+} in UiO-66-$(COOH)_2$-Cu (18 wt.%) into Cu_2O/Cu^0 during FAc reforming under visible light [20]. In this study, the formation of highly active Cu_2O/Cu^0 species trapped in the UiO-66 cages has been evidenced using high-resolution HAADF-STEM images and XPS. However, the detection of such Cu active species in Cu:Fe 1:2 photocatalyst was not possible due to its highly dispersion and/or low amount in respect to the Cu of the spinel-framework.

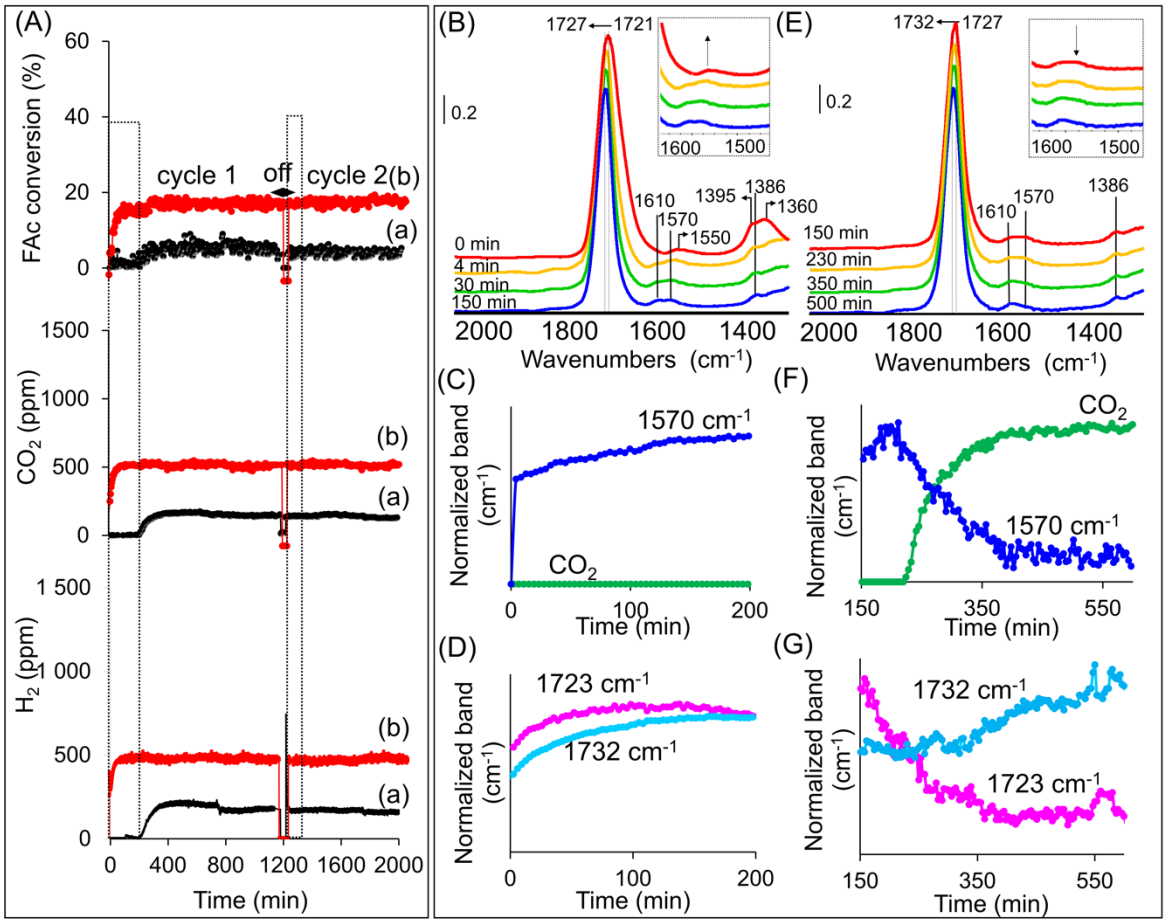

Figure 5. (A) Evolution of the FAc conversion (%) and the corresponding gas phase products (CO_2 and H_2) during the FA photo-reforming over (a) Cu_2O and (b) its mixture with Cu:Fe 1:3 under visible irradiation at RT. Evolution of the IR surface spectra of Cu_2O, the surface monodentate formate (1570 cm^{-1}) species vs. CO_2 production in gas phase and the band at 1721 vs. 1735 cm^{-1} during the induction period (B,C,D) and the photocatalytic cycle (E,F,G), respectively. Insert in B and E: zoom on the FTIR region of 1500-1600 cm^{-1}.

Operando-FTIR spectroscopy shed more light on the induction time as the evolution of the surface species is simultaneously monitored with the gas phase analysis during the reaction. Unfortunately, we were not able to monitor the surface of the Cu:Fe 1:2 photocatalyst due to depression of IR transmittance through the pellet once the lamp is turned on (Fig. S 10). It is probably due to the resonance saturation of IR absorption in semiconductors caused by the multiphoton inter-band absorption, spectral hole burning and carrier heating [41,42]. This phenomenon is less significant in case of less active Cu:Fe 1:3 in presence or absence of Cu_2O, but the spectra collected during the reaction are still not exploitable (Fig. S 11-12). For this reason, Cu_2O was chosen as a model to shed some light on the evolution of catalyst surface during the reaction. This allows to identify the reaction intermediates, to understand

454 the induction period and to propose a reaction mechanism over Cu:Fe 1:2 photocatalyst by
455 analogy with Cu_2O. The IR spectra of Cu_2O at different irradiation time were subtracted
456 from the one before FAc adsorption for clarity. The adsorption of FAc on Cu_2O
457 photocatalyst leads to the formation of new bands at 1550, 1360, 1395 and 2945 cm^{-1} (red
458 spectrum on Fig. 5B). Similar bands are observed on pure SiO_2 (Fig. S 13) and are attributed
459 to weakly adsorbed FAc [43]. The formation of an intense band at 1721 cm^{-1} parallel to the
460 decrease of Si-OH and/or Cu(OH) band at 3735 cm^{-1} is associated with the C=O stretching
461 mode of molecularly adsorbed FAc (Fig. S 13-14A). When the lamp is turned on, bands of
462 weakly adsorbed FAc (1360-1395 and 1550 cm^{-1}) disappear, while new features appear at
463 1386 and 1610-1570 cm^{-1} which can be assigned to the δ(CH) vibration of adsorbed
464 monodentate formate on copper [44]. These bands gradually increase during the induction
465 period without any production of CO_2 (Fig. 5C), indicating the rearrangement of adsorbed
466 formate on the photocatalyst surface. This is also confirmed by the increase in the carbonyl
467 band intensity at 1721 and 1732 cm^{-1} during the induction period (Fig. 5D). The absorption
468 at around 1732 cm^{-1} indicates either formation of weaker hydrogen bond with the FAc or
469 that FAc is in a less polar environment (surrounded by less -OH groups) [45,46] probably
470 caused by *in-situ* restructuring of Cu^{2+} into $Cu^{+/0}$ with less OH groups. A further decrease in
471 the band intensity of monodentate formate is also observed after 3 h of irradiation
472 accompanied by the production of CO_2 (Fig. 5E-F), which confirms the decomposition of
473 monodentate formate into CO_2 and H_2. During this photocatalytic cycle, a growth in the
474 band at 1732 cm^{-1} simultaneously to a decrease of the band located at 1721 cm^{-1} is also
475 observed (Fig. 5G), indicating the conversion of C=O groups from hydrogen-bonded to non
476 or less-hydrogen-bonded carbonyl groups during the reaction. These results allow, by
477 analogy with Cu_2O, to propose a plausible reaction mechanism over Cu:Fe 1:2 governing
478 the restructuring and the dissociation of FAc on the copper active sites, as detailed in the
479 next section.

In-situ restructuring of the Cu active sites in Cu:Fe 1:2

The crystallinity and optical properties of Cu_2O after photodecomposition of formic acid have been investigated by XRPD and DR-UV-Vis techniques (Fig. S 15). The results confirm a change of the catalyst in respect to the as-prepared sample and reveals the appearance of Cu characterized by diffraction peaks at 43.7, 50.7, and 74.3° and a Surface Plasmonic Resonance (SPR) absorption band at 566 nm [47,48,49]. The above results confirm that a part of the photoinduced electrons is not involved in the reaction during the induction period, i.e. rearrangement of formate species without H_2/CO_2 production in the first 3h, but is accumulated on the CB of photocatalyst to trigger the *in-situ* reduction and the restructuring process of Cu_2O into binary Cu_2O/Cu composite. Once the binary system is formed, the charge-carriers transport channel improves due to the enhanced charge separation and so the decomposition of formate species into CO_2 and H_2 occurs. This hypothesis is confirmed by testing under similar reaction condition an additional Cu_2O/Cu sample, which preparation is detailed in the experimental part. Higher activity (48% vs. 6%) and much shorter induction period were observed for Cu_2O/Cu in respect to Cu_2O (Table S2 and Fig. S 16). This confirms that the induction period is related to the restructuring of Cu_2O into Cu_2O/Cu and that the binary system exhibits higher photocatalytic activity. However, no direct evidence of the Cu formation was found in the case of Cu:Fe 1:2 after reaction (Fig. S 17), which is probably due to the high dispersion with low particle size and the relatively low amount of Cu active sites on this sample with respect to its total Cu content.

Additional XPS as well as the Cu $L_3M_{45}M_{45}$ Auger analyses of Cu:Fe 1:3 and 1:2 were performed in order to gain insight the environment of Cu and Fe in these photocatalytically inactive and active samples, respectively. The results reveal the absence of Cu^+ in both samples (Figures 6A and S 18). However, two types of coordination environments of Cu^{2+}

505 are detected: Cu^{2+} in octahedral (oct) sites (with Cu $2p_{3/2}$ and Cu $2p_{1/2}$ binding-energies at
506 933.5 and 953.5 eV, respectively) and a minor one for Cu^{2+} in tetrahedral (tet) coordination
507 with binding-energies of the Cu 2p doublet at 934.9 eV and 954.9 eV [50]. The
508 photoelectron peak contributions of both Cu^{2+} are colored in green and dark yellow while
509 their common satellites are colored in yellow in Fig. 6A. $Cu^{2+}{}_{tet}$ is ascribed to copper
510 coordinated with four oxygens, linked to two neighboring FeO_6 octahedra via corners to
511 form $[(Fe\text{-}O)_{2+x}\text{-}Cu(OH)_{2-x}]$ (with $0 \leq x \leq 2$)]. These species are more abundant in $CuFe_2O_4$
512 (Cu_{tet}/Cu_{oct} = 0.64) compared with Cu:Fe 1:3 (Cu_{tet}/Cu_{oct} = 0.47, Table S3). Also, $Fe^{3+}$and
513 Fe^{2+} oxidation states are detected by analyzing their Fe 2p spectra (Fig. 6A). The peak
514 contributions colored in yellow and green correspond to Fe 2p doublet and the satellites of
515 Fe^{3+} and Fe^{2+}, respectively [51]. The O 1s-spectrum can be fitted with three peak
516 contributions as the two low-energy peaks at 529.6 eV and 530.7 eV can be assigned to
517 bridging (Cu-O-Cu and Fe-O-Fe) and mixed bridging Cu-O-Fe bonds, respectively [52,53].
518 The third peak-contribution at 532.0 eV is usually attributed to oxygen in -O-H bonds, thus
519 confirming the interpretation given above for the presence of Cu-O-H bonding. The
520 $Cu^{2+}(OH)_2$, usually supported on different materials (TiO_2, ZnO/ZnS, $Fe(OH)_3$ and etc.), is
521 well known as an efficient co-catalyst for hydrogen production and easily reducible into
522 $Cu^{+/0}$ during the reaction [54,55,56].
523 Therefore, the photoelectrochemical properties of the Cu:Fe 1:2 were studied and compared
524 to the non-active Cu:Fe 1:3 sample (Fig. 6(B-C)). For Cu:Fe 1:3, the cyclic voltammetry
525 response, investigated in 0.1 M sodium sulfate solution at the potential window of 1.02 V-
526 0.0 V vs. RHE, demonstrates that the reduction/oxidation transitions of spinel are still well
527 distinguished either before or after 100 min of simulated solar irradiation. Moreover, an
528 obvious change in electrochemical behavior of Cu:Fe 1:2 after simulated solar irradiation is
529 observed. The intensity of the redox peaks associated with copper oxide decrease in
530 intensity compared to the as-prepared Cu:Fe 1:2 sample. On the other hand, the

electrochemical response of Cu:Fe 1:2 after irradiation shows higher anodic currents in the range between 0.68 V and 1.02 V vs. RHE than both Cu:Fe 1:2 and Cu:Fe 1:3 before irradiation and even than Cu:Fe 1:3 analyzed after induction period. This observation is probably attributed to gradual oxidation of Cu(I) oxide to Cu(II) hydroxide [57,58]. This confirms that, in contrast to Cu:Fe 1:3, the Cu^{+} species are formed in Cu:Fe 1:2 under visible light irradiation by an electron transfer (oxidation of formate species and/or from the photoexited spinel support). The transient photocurrent response tests under several on-off cycles of solar irradiation reveal as well a higher photoresponse efficiency of Cu:Fe 1:2 with regard to Cu:Fe 1:3 (Fig. 6C). It can be explained by the presence of higher amount of tetrahedral -$Cu^{2+}(OH)_{2-x}$ species in Cu:Fe 1:2 responsible for an efficient charge separation, therefore elucidating the superior photocatalytic activity of this photocatalyst. It is worth noting that no significant thermo-activity was observed in dark at 100°C over Cu:Fe 1:2 (Fig. S 19). This confirms that the reaction is mainly photocatalytic without excluding a plasmonic behavior due to the possible formation of Cu^{0}.

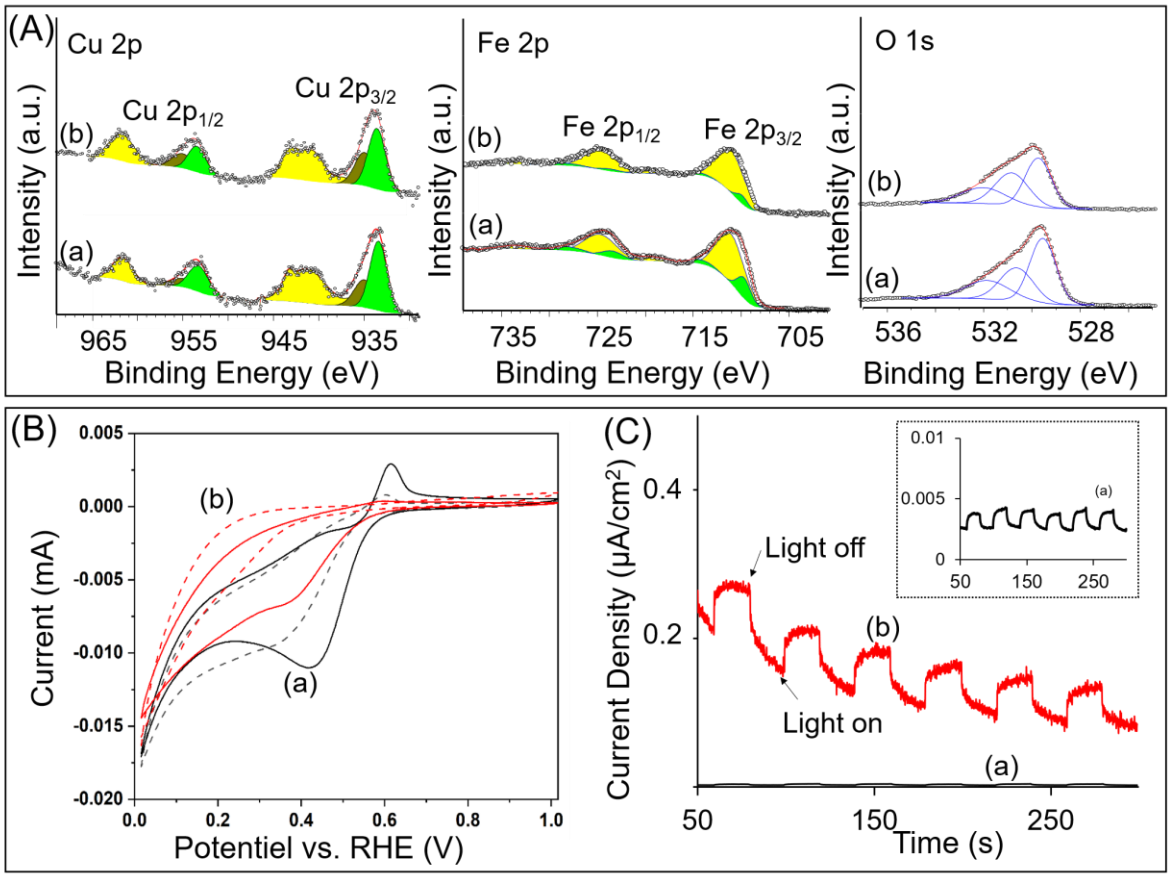

Figure 6. (A) High resolution XPS spectra of Cu 2p, Fe 2p and O1s for (a) Cu:Fe 1:3 and (b) Cu:Fe 1:2. (B) Cyclic voltammetry response of (a) Cu:Fe 1:3 and (b) Cu:Fe 1:2 electrode before (solid line) and after 100 min under simulated solar light irradiation (dash curve) in 0.1 mol.dm^{-3} Na_2SO_4 aqueous solution. (C) Plots of photocurrent *vs*. time recorded for (a) Cu:Fe 1:3 and (b) Cu:Fe 1:2. Insert: zoom on the photoresponse of Cu:Fe 1:3.

Based on the obtained results and by analogy with the various photocatalysts tested in this work, a plausible *in-situ* restructuring mechanism of the Cu:Fe 1:2 and the formation of ultra-dispersed photocatalytic active clusters during the induction period can be described as follows (Scheme 1): i) charge transfer and formation of surface formate species on the tetrahedral $Cu^{2+}(OH)_{2-x}$ active sites, ii) formation of Cu^{+} oxo species, promoted by a charge transfer from the spinel and followed by condensation and clustering of Cu with neighbor Cu^{+}-OH to form Cu_2O like clusters, iii) formation of Cu^{+} hydrides by dissociation of FAc accompanied by partial dissolution of surface copper, iv) subsequent CO_2 and H_2 production on Cu^{+} oxo and v) reductive hydride elimination on Cu^{+} oxalate leading to the formation of Cu^{+}/Cu^{0}.

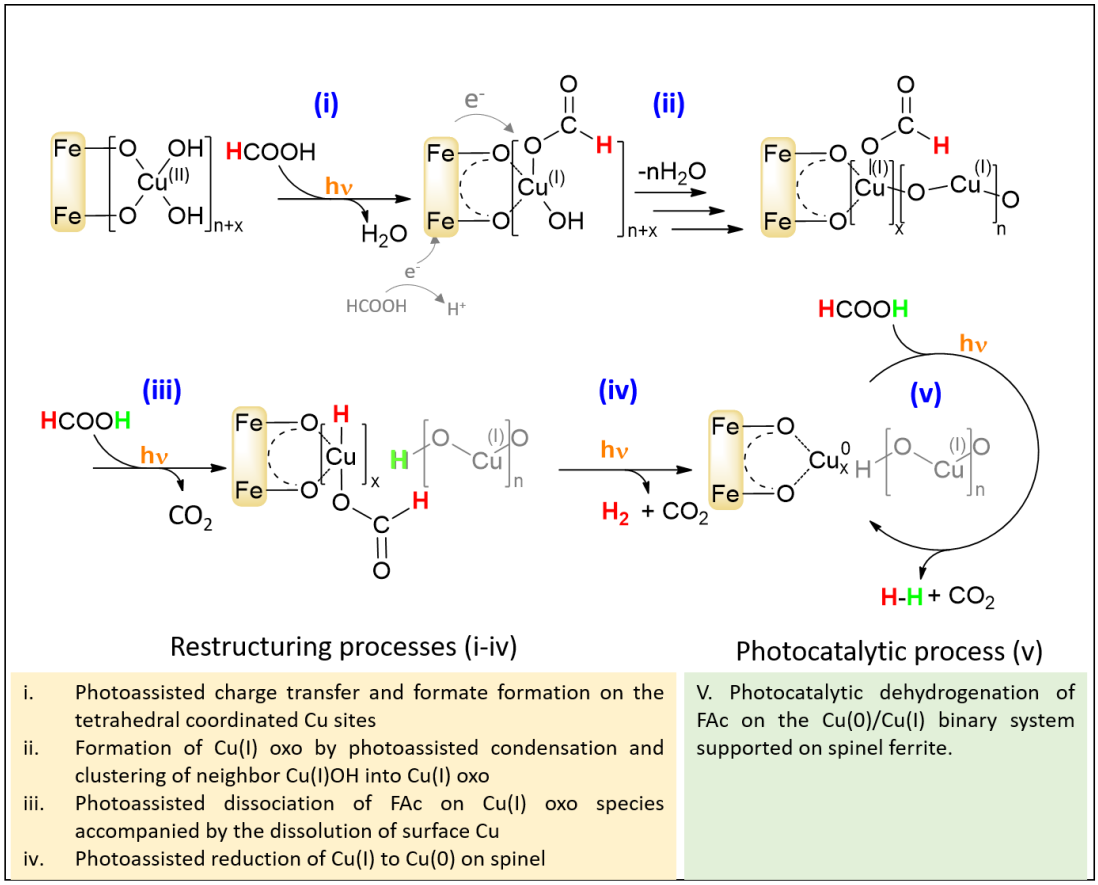

Scheme 1. Proposed mechanism of restructuring process of tetrahedral $Cu^{2+}(OH)_2$ active sites on Cu:Fe 1:2 during the photoreforming of formic acid under visible light irradiation.

Z-scheme heterojunction and charge transfer mechanism

In order to explain the charge separation mechanism, the positions of the conduction band (CB) and valence band (VB) of spinel in both Cu:Fe 1:3 and 1:2 photocatalysts were computed using the atom's Mulliken electronegativity equations with respect to the (NHE) scale [59,60]:

$$E_{VB} = X - E_e + {}^1/_2 E_g \quad (7)$$

$$E_{CB} = E_{VB} - E_g \quad (8)$$

Where E_{VB} is the VB potential, E_{CB} is the CB potential, E_e is the energy of free electrons on the hydrogen scale (ca. 4.5 eV), E_g is the band gap energy of spinel (1.90 for Cu:Fe 1:3 and 1.85 eV for Cu:Fe 1:2, Fig. S 4) and X is the absolute electronegativity of the copper iron spinel (5.86 eV [61,62]). On the basis of the above equations, the E_{VB} and E_{CB} of Cu:Fe 1:3 were calculated with respect to NHE as + 2.31 V and + 0.41 V, whereas the potentials for 1:2 sample were estimated to + 2.28 V and + 0.43 V, respectively. Consequently, the

hydrogen reduction cannot take place on Cu:Fe 1:3 due to its unsuitable CB position (+ 0.41 V) compared to H^+/H_2 potential (-0.18 V vs. NHE at pH = 3; 0.0 V vs. RHE). Considering that Cu:Fe 1:2 contains -$Cu^{2+}(OH)_2$ active species that are restructured into Cu^+ and Cu^0, an efficient charge separation mechanism can be proposed by assuming that Cu^+ of the Cu:Fe 1:2 is similar to Cu_2O (scheme 2): Under visible light (λ>390 nm), the excited electrons are transferred from the VB of the spinel to its CB thereby oxidizing FAc mainly into CO_2 (with a small amount of CO) and H^+ by combination with the photogenerated holes of spinel. Simultaneously, the electrons accumulated on $Cu^{2+}(OH)_{2-x}$ are involved in the reduction and *in situ* restructuring of Cu^{2+} (scheme 1) into trinary Cu^+/Cu^0/spinel Z-scheme heterojunction (scheme 2), promoting then the proton reduction into H_2.

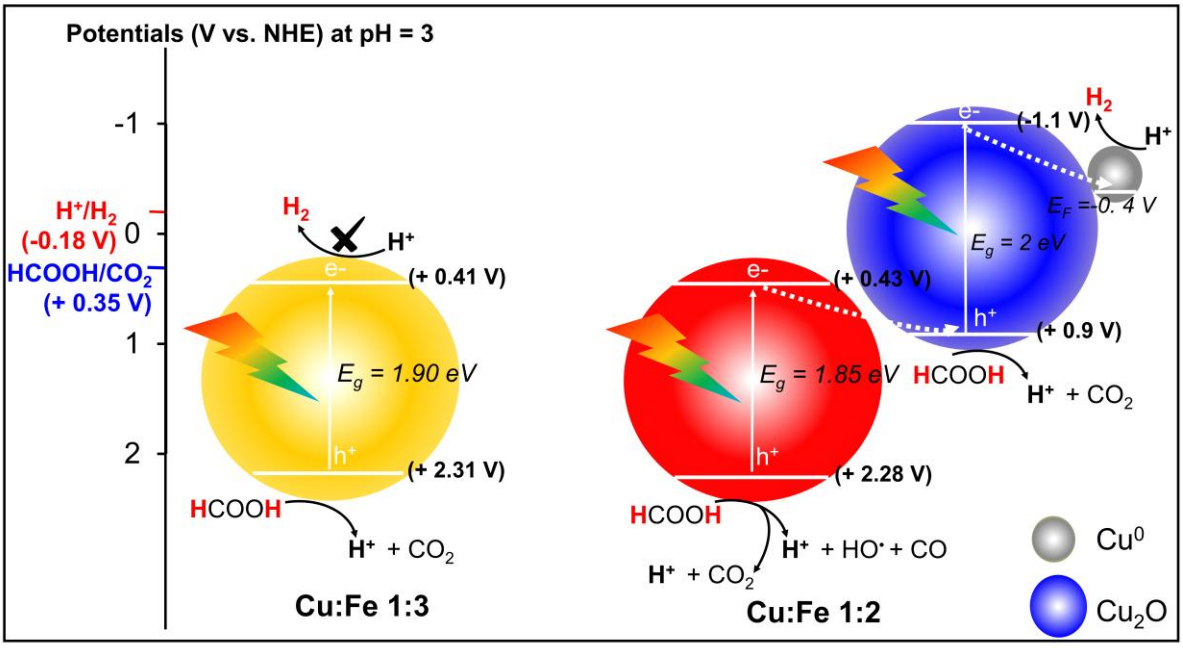

Scheme 2. Schematic diagram showing the photoinduced charge-carriers transfer and the H_2 production through the photodecomposition of formic acid under visible light over Cu:Fe 1:3 and Cu:Fe 1:2.

4. Conclusion

The H_2 production via photoreforming of FAc is studied in vapor phase under continuous flow over low-cost $CuFe_2O_4$-based photocatalyst under visible light (λ> 390 nm) and at room temperature. The influence of Cu:Fe ratio on the photocatalytic activity was

investigated. We demonstrated that nor spinel with equal or lower Cu:Fe ratio than 1:3, neither those treated below 700°C are photocatalytically active under visible light irradiation. By contrast, a synergetic activity is observed for $CuFe_2O_4$ (Cu:Fe 1:2) once annealed at 800 °C. This photocatalyst exhibits the highest hydrogen production rate (~ 6.6 $mmol.g^{-1}.h^{-1}$), with an apparent quantum yield equal to 7.3%, together with a relatively good dehydrogenation-selectivity (77 %) and ultra-high stability (> 20 h) compared to other copper-based systems investigated in the literature. As confirmed by XPS, this excellent photocatalytic behavior is attributed to the existence of highly dispersed tetrahedral-$Cu^{2+}(OH)_{2-x}$ sites on the spinel surface. Based on the presence of an induction period in the first cycle of reaction and by analogy with other Cu_2O based photocatalyst and Cu based oxides, an *in-situ* restructuring of tetrahedral Cu^{2+} into a trinary (Cu^{+}/Cu^{0}/spinel) with Z-scheme heterojunction is proposed, promoting the electron/holes charge separation and thus the proton reduction into H_2. Although the selectivity of the reaction is lower than the one reported in our previous work using Cu/MOFs based catalyst, the high activity observed for the $CuFe_2O_4$ photocatalyst, its low cost and its simple synthesis procedure motivate investigating new Cu-Fe based materials for various applications in photocatalysis under visible light.

Author Contributions

†These authors contributed equally. The manuscript was prepared written through the contributions of all authors. All authors have approved the final version of the manuscript.

ACKNOWLEDGMENT

Authors acknowledge the Normandy region (H_2CO_2 project) for the financial support. JPB, AM and CM acknowledge the financial support of the French Agence Nationale de la Recherche LabEx EMC3 through the Project MaPhoOBi (Grant No. ANR-10-LABX-09-01), and the Normandy Region (RIN - Label d'Excellence). AP also thanks the financial support of the Normandy Region (AAP RIN RECHERCHE 2018: DIXOS 2018DRI00029). Authors acknowledge Jaafar El FALLAH for the SEM-EDX analysis and Oleg Lebedev for the TEM analysis.

629
630 **References**

[1] L. Van Hoecke, L. Laffineur, R. Campe, P. Perreault, S.W. Verbruggen & S. Lenaerts. Challenges in the use of hydrogen for maritime applications. *Energy & Environ. Sci*. 14(2021)815-843. https://doi.org/10.1039/D0EE01545H.

[2] M. Yadav, & Q. Xu. Liquid-phase chemical hydrogen storage materials. *Energy & Environ. Sci.* 5(2012) 9698-9725. https://doi.org/10.1039/C2EE22937D.

[3] D. Mellmann, P. Sponholz, H. Junge, & M. Beller. Formic acid as a hydrogen storage material–development of homogeneous catalysts for selective hydrogen release. *Chem. Soc. Rev*. 45(2016)3954-3988. https://doi.org/10.1039/C5CS00618J.

[4] M. Navlani-García, D. Salinas-Torres, K. Mori, Y. Kuwahara & H. Yamashita. 2020, Photocatalytic approaches for hydrogen production via formic acid decomposition. Heterogeneous Photocatalysis, 193-223.

[5] M. El-Roz, I. Telegeiev, N.E. Mordvinova, O.I. Lebedev, N. Barrier, A. Behilil & V. Valtchev. Uniform generation of sub-nanometer silver clusters in zeolite cages exhibiting high photocatalytic activity under visible light. *ACS Appl. Mater. Interfaces.* 10(2018)28702-28708. https://doi.org/10.1021/acsami.8b09634.

[6] M. Navlani-García, I. Miguel-García, Á. Berenguer-Murcia, D. Lozano-Castelló, D. Cazorla-Amorós & H. Yamashita. Pd/zeolite-based catalysts for the preferential CO oxidation reaction: ion-exchange, Si/Al and structure effect. Catal. Sci. & Technol. 6(2016)2623-2632. https://doi.org/10.1039/C5CY02044A.

[7] Z. Li, X. Yang, N. Tsumori, Z. Liu, Y. Himeda, T. Autrey & Q. Xu. Tandem nitrogen functionalization of porous carbon: Toward immobilizing highly active palladium nanoclusters for dehydrogenation of formic acid. *ACS Catal*. 7 (2017) 2720-2724. https://doi.org/10.1021/acscatal.7b00053.

[8] B. Gholipour, A. Zonouzi, M. Shokouhimehr, & S. Rostamnia, S. Integration of plasmonic AgPd alloy nanoparticles with single-layer graphitic carbon nitride as Mott-Schottky junction toward photo-promoted H_2 evolution. *Sci. Rep.12*(2022) 1-13. https://doi.org/10.1038/s41598-022-17238-4.

[9] N. Nouruzi, M. Dinari, B. Gholipour, N. Mokhtari, M. Farajzadeh, S. Rostamnia & M. Shokouhimehr. Photocatalytic hydrogen generation using colloidal covalent organic polymers decorated bimetallic Au-Pd nanoalloy (COPs/Pd-Au). *Mol. Catal. 518* (2022) 112058. https://doi.org/10.1016/j.mcat.2021.112058.

[10] R. Xu, W. Lu, S. Toan, Z. Zhou, C. K. Russell & Z. Sun. Thermocatalytic formic acid dehydrogenation: recent advances and emerging trends. *J. Mater. Chem. A*. 9(2021) 24241-24260. https://doi.org/10.1039/D1TA05910F.

[11] J. A. Nasir, M. Hafeez, M. Arshad, N.Z. Ali, I. F. Teixeira, I. McPherson & M. A. Khan. Photocatalytic dehydrogenation of formic acid on CdS nanorods through Ni and Co redox mediation under mild conditions. *ChemSusChem*, 11(2018)2587-2592. https://doi.org/10.1002/cssc.201800583.

[12] S. Duan, S. Zhang, S. Chang, S. Meng, Y. Fan, X. Zheng & S. Chen. Efficient photocatalytic hydrogen production from formic acid on inexpensive and stable phosphide/$Zn_3In_2S_6$ composite photocatalysts under mild conditions. *Int. J. Hydrog. Energy*. 44(2019)21803-21820. https://doi.org/10.1016/j.ijhydene.2019.06.179.

[13] A. Ahadi, H. Alamgholiloo, S. Rostamnia, X. Liu, M. Shokouhimehr, D. A. Alonso & R. Luque. Layer- Wise Titania Growth Within Dimeric Organic Functional Group Viologen Periodic Mesoporous Organosilica as Efficient Photocatalyst for Oxidative Formic Acid Decomposition. *ChemCatChem*, *11*(2019), 4803-4809. https://doi.org/10.1002/cctc.201900486.

[14] H. M. Yeh, S. L. Lo, M. J. Chen & H. Y. Chen. Hydrogen production from formic acid solution by modified TiO_2 and titanate nanotubes in a two-step system under visible light irradiation. *Water Sci. Technol*. 69(2014) 1676-1681. https://doi.org/10.2166/wst.2014.072.

[15] X. Wang, W. C. Peng & X. Y. Li. Photocatalytic hydrogen generation with simultaneous organic degradation by composite CdS–ZnS nanoparticles under visible light. *Int. J. Hydrog. Energy*. 39(2014)13454-13461. http://dx.doi.org/10.1016/j.mseb.2013.11.015.

[16] M. Zeng, Z. Chai, X. Deng, Q. Li, S. Feng, J. Wang & D. Xu. Core–shell CdS@ ZIF-8 structures for improved selectivity in photocatalytic H_2 generation from formic acid. *Nano Res.* 9(2016)2729-2734. https://doi.org/10.1007/s12274-016-1161-3.

[17] S. Kakuta & T. Abe. A novel example of molecular hydrogen generation from formic acid at visible-light-responsive photocatalyst. *ACS Appl. Mater. Interfaces.* 1(2009)2707-2710. https://doi.org/10.1021/am900707e.

[18] Z. Zhang, K. Liu, Y. Bao & B. Dong. Photo-assisted self-optimizing of charge-carriers transport channel in the recrystallized multi-heterojunction nanofibers for highly efficient photocatalytic H_2 generation. *Appl. Catal. B: Environ.* 203(2017)599-606. https://doi.org/10.1016/j.apcatb.2016.10.064

[19] M. I. Maldonado, E. Saggioro, J. Peral, E. Rodríguez-Castellón, J. Jiménez-Jiménez & S. Malato. Hydrogen generation by irradiation of commercial CuO+ TiO_2 mixtures at solar pilot plant scale and in

presence of organic electron donors. *Appl. Catal. B: Environ.* 257(2019)117890. https://doi.org/10.1016/j.apcatb.2019.117890.
[20] H. Issa Hamoud, P. Damacet, D. Fan, N. Assaad, O. Lebedev, A. Krystianiak, O. Heintz, M. Daturi, G. Maurin, M. Hmadeh, M. El-Roz. Selectively photocatalytic dehydrogenation of formic acid by in situ restructured copper post-metalated metal organic framework under visible light. *J. Am. Chem. Soc.* (2022) https://doi.org/10.1021/jacs.2c04905.
[21] K. Shetty, L. Renuka, H.P. Nagaswarupa, H. Nagabhushana, K.S. Anantharaju, D. Rangappa, S.C. Prashantha, K. Ashwini, A comparative study on $CuFe_2O_4$, $ZnFe_2O_4$ and $NiFe_2O_4$: morphology, impedance and photocatalytic studies. *Mater. Today Proc.* 4(2017)11806–11815. https://doi.org/10.1016/J.MATPR.2017.09.098.
[22] I. Nedkov, R.E. Vandenberghe, T. Marinova, P. Thailhades, T. Merodiiska, & I. Avramova. Magnetic structure and collective Jahn–Teller distortions in nanostructured particles of $CuFe_2O_4$. *Appl. Surf. Sci.253*(2006) 2589-2596. https://doi.org/10.1016/j.apsusc.2006.05.049.
[23] B. J. Evans & S. S. Hafner. Mössbauer resonance of Fe^{57} in oxidic spinels containing Cu and Fe. *J. Phys. Chem. Solids. 29* (1968)1573-1588. https://doi.org/10.1016/0022-3697(68)90100-5.
[24] Y. Zhao, C. Lin, H. Bi, Y. Liu, Q. Yan. Magnetically separable $CuFe_2O_4$/AgBr composite photocatalysts: Preparation, characterization, photocatalytic activity and photocatalytic mechanism under visible light. Appl. Surf. Sci., 392 (2017)701-707. https://doi.org/10.1016/J.APSUSC.2016.09.099.
[25] B. S. Surendra. Green engineered synthesis of Ag-doped $CuFe_2O_4$: characterization, cyclic voltammetry and photocatalytic studies. *J. Sci.: Adv. Mater. Devices.* 3(2018)44-50. https://doi.org/10.1016/j.jsamd.2018.01.005.
[26] H. Astaraki, S. M. Masoudpanah, S. Alamolhoda. Effects of ethylene glycol contents on phase formation, magnetic properties and photocatalytic activity of $CuFe_2O_4$/Cu_2O/Cu nanocomposite powders synthesized by solvothermal method. J. Mater. Res. Technol. 14(2021)229-241. https://doi.org/10.1016/j.jmrt.2021.06.046.
[27] A. Massoud-Sharifi, G. K. Kara & M. Rabbani. 2019. $CuFe_2O_4$@ CuO: a magnetic composite synthesized by ultrasound irradiation and degradation of methylene blue on its surface in the presence of sunlight. In Multidisciplinary Digital Publishing Institute Proceedings, vol. 48, p. 17.
[28] H. Yang, J. Yan, Z. Lu, X. Cheng & Y. Tang. Photocatalytic activity evaluation of tetragonal $CuFe_2O_4$ nanoparticles for the H_2 evolution under visible light irradiation. *J. Alloys Compd.* 476(2009)715-719. https://doi.org/10.1016/j.jallcom.2008.09.104.
[29] R. S. Yadav, J. Havlica, I. Kuřitka, Z. Kozakova, M. Palou, E. Bartoníčková & J. Wasserbauer. Magnetic properties of ZnFe2O4 nanoparticles synthesized by starch-assisted sol–gel auto-combustion method. *J. Supercond. Nov. Magn.* 28(2015)1417-1423. https://doi.org/10.5772/intechopen.72864.
[30] J. Zhu, H. Bi, Y. Wang, X. Wang, X. Yang & L. Lu. CuO nanocrystals with controllable shapes grown from solution without any surfactants. *Mater. Chem. Phys.* 109(2008)34-38. https://doi.org/10.1016/j.matchemphys.2007.10.027.
[31] R. Kumar, P. Rai & A. Sharma. Facile synthesis of Cu_2O microstructures and their morphology dependent electrochemical supercapacitor properties. *RSC. Advances.* 6(2016)3815-3822. https://doi.org/10.1039/C5RA20331G.
[32] L. Vivas, I. Chi-Duran, J. Enríquez, N. Barraza & D. P. Singh, D. P. Ascorbic acid based controlled growth of various Cu and Cu_2O nanostructures. *Mat. Res. Exp. 6*(2019)065033. https://doi.org/10.1088/2053-1591/ab0dd2.
[33] M. El-Roz, M. Kus, P. Cool & F. Thibault-Starzyk. New operando IR technique to study the photocatalytic activity and selectivity of TiO_2 nanotubes in air purification: influence of temperature, UV intensity, and VOC concentration. *J. Phys. Chem. C.* 116(2012)13252-1326. https://doi.org/10.1021/jp3034819.
[34] M. El-Roz, P. Bazin & F. Thibault-Starzyk. An operando-IR study of photocatalytic reaction of methanol on new* BEA supported TiO_2 catalyst. *Catal. Today.* 205(2013)111-119. https://doi.org/10.1016/j.cattod.2012.08.023.
[35] T. Inoue & S. Iida. Specific Heats of Copper Ferrite. *J. Phys. Soc. Jpn.* 13(1958)656A-656A. https://doi.org/10.1143/JPSJ.13.656A.
[36] W. O. Milligan and J. Holmes. X-Ray Diffraction Studies in the System CuO-Fe_2O_3. *J. Am. Chem. Soc.* 63 (1941) 149-150. https://pubs.acs.org/doi/pdf/10.1021/ja01846a036.
[37] S. Park, J. H. Baek, L. Zhang, J. M. Lee, K. H. Stone, I. S. Cho & X. Zheng. Rapid flame-annealed $CuFe_2O_4$ as efficient photocathode for photoelectrochemical hydrogen production. ACS Sustain. Chem. Eng. 7(2019)5867-5874. https://doi.org/10.1021/acssuschemeng.8b05824.
[38] A. N. Pestryakov, V. P. Petranovskii, A. Kryazhov, O. Ozhereliev, N. Pfänder & A. Knop-Gericke. Study of copper nanoparticles formation on supports of different nature by UV–Vis diffuse reflectance spectroscopy. *Chem. Phys. Lett.* 385(2004)173-176. https://doi.org/10.1016/j.cplett.2003.12.077.

[39] Y. F.Lim, J. J. Choi & T. Hanrath. Facile synthesis of colloidal CuO nanocrystals for light-harvesting applications. *J. Nanomat*. (2012)*2012*. https://doi.org/10.1155/2012/393160.
[40] K. Jung, T. Lim, H. Bae, J.S. Ha & A. A. Martinez- Morales. Cu_2O photocathode with faster charge transfer by fully reacted cu seed layer to enhance performance of hydrogen evolution in solar water splitting applications. *ChemCatChem*, *11*(2019), 4377-4382. https://doi.org/10.1002/cctc.201900526.
[41] L. G. Gerchikov, D. A. Parshin & A. R. Shabaev. Theory of resonance saturation of IR absorption in semiconductors with degenerate resonance bands in electric and magnetic fields. *Zh. Eksp. Teor. Fiz.* 96(1989)1046.
[42] A. O. Melikyan & G. R. Minasyan. Saturation of interband absorption in semiconductors. *Semiconductors*. 34(2000)386-388. https://doi.org/10.1134/1.1187993.
[43] G. J. Millar, C. H. Rochester & K. C. Waugh. Infrared study of the adsorption of formic acid on silica-supported copper and oxidised copper catalysts. *J. Chem. Soc. Faraday Trans.* 87(1991)1491-1496. https://doi.org/10.1039/FT9918701491.
[44] T. F. Pascher, M. Ončák, C. van der Linde & M.K. Beyer. Infrared multiple photon dissociation spectroscopy of anionic copper formate clusters. *Chem. Phys.* 153(2020)184301. https://doi.org/10.1063/5.0030034.
[45] K. Thumanu, J. Cha, J. F. Fisher, R. Perrins, S. Mobashery, & C. Wharton. 2006. Discrete steps in sensing of β-lactam antibiotics by the BlaR1 protein of the methicillin-resistant Staphylococcus aureus bacterium. Proceedings of the National Academy of Sciences, 103, 10630-10635.
[46] L. B. Dreier, M. Bonn & E. H. Backus, E. H. Hydration and orientation of carbonyl groups in oppositely charged lipid monolayers on water. *J. Phys. Chem. B.* 123(2019)1085-1089. https://doi.org/10.1021/acs.jpcb.8b12297.
[47] R. Betancourt-Galindo, P. Y. Reyes-Rodriguez, B. A. Puente-Urbina, C. A. Avila-Orta, O. S. Rodríguez-Fernández, G. Cadenas-Pliego & L. A. García-Cerda, L. A. Synthesis of copper nanoparticles by thermal decomposition and their antimicrobial properties. *J. Nanomater.* 2014(2014). https://doi.org/10.1155/2014/980545.
[48] G. K. Inwati, Y. Rao & M. Singh. Thermodynamically induced in situ and tunable Cu plasmonic behaviour. *Sci. Rep*. 8(2018)1-15. https://doi.org/10.1038/s41598-018-20478-y.
[49] D. Mott, J. Galkowski, L. Wang, J. Luo & C. J. Zhong. Synthesis of size-controlled and shaped copper nanoparticles. *Langmuir*. 23(2007)5740-5745. https://doi.org/10.1021/la0635092.
[50] Z. Ye, Z. Deng, L. Zhang, J. Chen, G. Wang & Z. Wu. The structure of copper ferrite prepared by five methods and its catalytic activity on lignin oxidative degradation. *Mater. Res. Expres.* 7(2020)035007. https://doi.org/10.1088/2053-1591/ab778b.
[51] T. Yamashita, P. Hayes, Analysis of XPS spectra of Fe^{2+} and Fe^{3+} ions in oxide materials, *Appl. Surf. Sci.* 254(2008)2441–2449. https://doi.org/10.1016/j.apsusc.2007.09.063.
[52] A. Losev, K. Kostov, G. Tyuliev, Electron beam induced reduction of CuO in the presence of a surface carbonaceous layer: an XPS/HREELS study. *Surf. Sci*. 213(1989)564-579. https://doi.org/10.1016/0039-6028(89)90313-0.
[53] T. Yamashita, P. Hayes, Analysis of XPS spectra of Fe^{2+} and Fe^{3+} ions in oxide materials. *Appl. Surf. Sci.* 254(2008)2441–2449. https://doi.org/10.1016/j.apsusc.2007.09.063.
[54] J. Yu & J. Ran. Facile preparation and enhanced photocatalytic H_2-production activity of Cu $(OH)_2$ cluster modified TiO_2. *Energy Environ. Sci.* 4(2011)1364-1371. https://doi.org/10.1039/C0EE00729C.
[55] P. Madhusudan, Y. Wang, B. N. Chandrashekar, W. Wang, J. Wang, J. Miao & C. Cheng. Nature inspired ZnO/ZnS nanobranch-like composites, decorated with Cu $(OH)_2$ clusters for enhanced visible-light photocatalytic hydrogen evolution. *Appl. Catal. B: Environ.* 253(2019)379-390. https://doi.org/10.1016/j.apcatb.2019.04.008.
[56] C. Y. Peng, C. C. Hou, Q. Q. Chen, C. J. Wang, X. J. Lv, J. Zhong & Y. Chen. Cu $(OH)_2$ supported on Fe $(OH)_3$ as a synergistic and highly efficient system for the dehydrogenation of ammonia-borane. *Sci. Bull.* 63(23)1583-1590. https://doi.org/10.1016/j.scib.2018.11.003.
[57] R. Wick & S. D. Tilley. Photovoltaic and photoelectrochemical solar energy conversion with Cu_2O. *J. Phys. Chem. C.* 119(2015) 26243-26257. https://doi.org/10.1038/srep30882.
[58] W. Kautek & J. G. Gordon. XPS studies of anodic surface films on copper electrodes. *J. Electrochem. Soc.* 137(1990) 2672. https://doi.org/10.1149/1.2087008.
[59] K. Jahanara & S. Farhadi. A magnetically separable plate-like cadmium titanate–copper ferrite nanocomposite with enhanced visible-light photocatalytic degradation performance for organic contaminants. *RSC adv*. 9(2019)15615-15628. https://doi.org/10.1039/C9RA01968E.
[60] S. Shenoy & K. Tarafder. Enhanced photocatalytic efficiency of layered CdS/CdSe heterostructures: Insights from first principles electronic structure calculations. *Journal of Physics: Cond. Matter*. *32*(2020) 275501.

[61] J. H.Tan, J. C. Sin & S. M. Lam. Synthesis of Z-scheme BiOCI/$CuFe_2O_4$ Composite with Enhanced Visible Light Photodegradation of Palm Oil Mill Effluent. *IOP Conf. Ser.: Earth Environ. Sci*. 945(2021)012034. https://doi.org/10.1088/1755-1315/945/1/012034.
[62] Y. Xu & M. A. Schoonen. The absolute energy positions of conduction and valence bands of selected semiconducting minerals. *Am. Mineral. 85*(2000)543-556. https://doi.org/10.2138/am-2000-0416.